IOP Publishing Nanotechnology 37 (2026) 035001 https://doi.org/10.1088/1361-6528/ae2d5e

Nanotechnology

OPEN ACCESS

RECEIVED
23 September 2025

REVISED
4 December 2025

ACCEPTED FOR PUBLICATION
16 December 2025

PUBLISHED
19 January 2026

PAPER

Magnetic ordering in moiré graphene multilayers from a continuum Hartree+U approach

Christopher T S Cheung[1], **Valerio Vitale**[1,2,3], **Lennart Klebl**[4], **Ammon Fischer**[5,6], **Dante M Kennes**[5,6], **Arash A Mostofi**[1], **Johannes Lischner**[1] **and Zachary A H Goodwin**[1,7,8,*]

[1] Departments of Physics and Materials and the Thomas Young center for Theory and Simulation of Materials, Imperial College London, South Kensington Campus, London SW7 2AZ, United Kingdom
[2] Dipartimento di Fisica, Università degli Studi di Trieste, strada costiera 11, 34151 Trieste, Italy
[3] CNR-IOM–Istituto Officina dei Materiali, National Research Council of Italy, c/o SISSA Via Bonomea 265, Trieste IT-34136, Italy
[4] Institut für Theoretische Physik und Astrophysik and Würzburg-Dresden Cluster of Excellence ct.qmat, Universität Würzburg, 97074 Würzburg, Germany
[5] Max Planck Institute for the Structure and Dynamics of Matter, Center for Free Electron Laser Science, 22761 Hamburg, Germany
[6] Institute for Theory of Statistical Physics, RWTH Aachen University, and JARA Fundamentals of Future Information Technology, 52062 Aachen, Germany
[7] John A. Paulson School of Engineering and Applied Sciences, Harvard University, Cambridge, MA 02138, United States of America
[8] Department of Materials, University of Oxford, Parks Road, Oxford OX1 3PH, United Kingdom
[*] Author to whom any correspondence should be addressed.

E-mail: zac.goodwin@materials.ox.ac.uk

Keywords: twisted bilayer graphene, magnetism, atomistic, continuum

Supplementary material for this article is available online

Abstract

Recently, symmetry-broken ground states, such as correlated insulating states, magnetic order and superconductivity, have been discovered in twisted bilayer graphene (tBLG) and twisted trilayer graphene (tTLG) near the so-called magic angles. Understanding the magnetic order in these systems is challenging, however, as atomistic methods become extremely expensive near the magic angle and continuum approaches fail to capture important atomistic details. In this work, we develop an approach to incorporate short-ranged Hubbard interactions self-consistently in a continuum model. In addition, we include long-ranged Coulomb interactions which are known to be important when doping the flat bands of tBLG and tTLG. Therefore, for the first time, magnetic order in moiré graphene multilayers is self-consistently explored in a continuum model with atomistic detail. With this approach, we perform a systematic analysis of the magnetic phase diagram of tBLG as a function of doping level and twist angle, near the magic angle. Our results are consistent with previous perturbative atomistic Hartree+U calculations. Furthermore, we investigated magnetic order of tTLG, which were found to be similar to those in tBLG. In the future, the developed continuum model can be utilized to investigate magnetic ordering tendencies from short-range exchange interactions in other moiré graphene multilayers as a function of doping, twist angle, screening environment, among other variables.

1. Introduction

Since the discovery of correlated insulating states [1] and superconductivity [2] in magic-angle twisted bilayer graphene (tBLG), moiré materials have emerged as an excellent platform for understanding flat-band physics and strongly-correlated electrons. This is demonstrated by the unprecedented variety of exotic electronic states that have been experimentally observed in tBLG, such as global charge-ordered stripe phases [3], ferromagnetic (FM) chiral edge states [4], orbital magnetism [5], among other experimental and theoretical findings [3, 5–35]. After these discoveries, flat-band physics and strong correlations have been discovered in moiré materials other than tBLG. For example, still using graphene as a building block, twisted trilayer graphene [36, 37] (tTLG), twisted double bilayer graphene (tDBLG) [38–41], among other systems [42], have been actively investigated, and correlated insulating states and superconductivity have also been found. Moreover, this prompted multilayer graphene systems without a twist to be revisited, leading, for instance, to the discovery of superconductivity and magnetism in rhombohedral graphene multilayers [43–49]. In addition to twisted graphitic materials, twisted bilayers and multilayers consisting of other 2D materials have also been investigated, such as semiconducting transition metal dichalcogenides (TMDs) [50–55], metallic TMDs [56, 57], hexagonal boron nitride [58, 59], among other examples [30].

In tBLG, flat bands near the Fermi energy were predicted by Bistrizer and MacDonald's continuum model at specific twist angles, referred to as magic angles [60]. Since the discovery of broken symmetry states at the $\sim 1.1^\circ$ magic angle, theoretical effort has largely focused on incorporating interactions into the electronic Hamiltonian of this continuum model, in an attempt to understand these phases. Notably, Guinea *et al* incorporated long-ranged Hartree interactions into the continuum model, predicting strong distortions of the flat bands near the magic angle [61–64]. Long-ranged exchange, i.e. Fock, interactions have also been included in the continuum model, giving rise to various broken symmetry states in reasonable agreement with experimental measurements [23, 63, 64]. Alternative approaches based on the Wannier functions of the flat bands have also had success in explaining experimental measurements [10, 65–69]. However, neither of these techniques has clearly determined the role of short-ranged interactions, as separating the effects of short-range and long-range interactions in these methods is difficult.

Atomistic models, on the other hand, can naturally include short-ranged interactions, such as the onsite repulsion between electrons in p_z orbitals [70–73]. The magnetic phases of tBLG have been studied using atomistic perturbative random phase approximation (RPA) calculations at the magic angle by Klebl *et al* [74–76], which predicted the existence of emergent moiré-scale modulated antiferromagnetic and FM states [74]. Klebl *et al* [74, 75] also mapped the magnetic phase diagram of tBLG over a range of twist angles at integer doping levels up to ±3 electrons per moiré unit cell, taking into account long-ranged Hartree interactions (in a perturbative way) [75]. However, a major challenge presented by atomistic tight-binding approaches is the computational cost of reaching converged solutions for small twist-angle systems [70–73]. Motivated by the low computational cost of continuum models, and the success of atomistic models in capturing short-ranged interactions, Jimeno-Pozo *et al* [77] developed a hybrid approach to incorporate atomistic onsite p_z Hubbard interactions into the continuum model [74, 75]. The magnetic orders predicted by the atomistic models were incorporated into the continuum model through a sublattice-polarized moiré expansion, similar to how Hartree interactions are included in the continuum model [77]. Those calculations, however, were only perturbative.

In this work, we develop and perform self-consistent Hartree+U calculations in the continuum model of moiré graphene multilayers. Using this methodology, we compute the self-consistent order parameters of several magnetic instabilities over a range of integer doping levels in the flat bands and a range of twist angles near the magic angle. These calculations provide insight into the regions of stability for each competing magnetic state in tBLG. The developed approach is general, which we demonstrate by predicting quasiparticle band structures for symmetric tTLG with different magnetic orders, where we found similarities to tBLG. We hope this method will open up avenues to include both short and long range exchange interactions, to determine their relative importance. Moreover, the developed method could also be used for other moiré graphene multilayers, or moiré systems comprising of other 2D materials.

2. Methods

We develop a combined atomistic–continuum approach here. First, we determine the leading magnetic instabilities using an RPA theory based on the atomistic tight-binding model. As these magnetic instabilities have already been discussed in depth elsewhere, we refer the reader to references [74, 75] for the details of these calculations. These leading magnetic instabilities are then included in the continuum model by approximating their form with a sum of trigonometric functions. The reader should refer to reference [77] for a more detailed description of this procedure. In the remainder of the methods section, we outline the self-consistent continuum model approach developed here, which builds on the previously mentioned work.

2.1. Continuum model for tBLG

The atomic structure of tBLG is obtained by rotating the top and bottom layers by $\pm\theta/2$, where θ is the twist angle. As we build on atomistic methods, we choose twist angles with commensurate moiré unit cells, described by the moiré lattice vector $\mathbf{R}_1 = m\mathbf{a}_1 + n\mathbf{a}_2$, with (m, n) being non-equal integers, and $\mathbf{a}_1 = (\sqrt{3}/2, -1/2)a_0$, $\mathbf{a}_2 = (\sqrt{3}/2, 1/2)a_0$ are the graphene unit cell vectors. The lattice constant a_0 is taken as 2.46 Å.

The low-energy electronic properties of tBLG, without any electron–electron interactions, are described with a Bistritzer-MacDonald continuum model [60]

$$\mathcal{H}_0^{\chi}(\mathbf{k};\theta) = \begin{pmatrix} \mathcal{H}^{1,\chi}(\mathbf{k};\theta) & \mathcal{U}^{\chi,\dagger} \\ \mathcal{U}^{\chi} & \mathcal{H}^{2,\chi}(\mathbf{k};\theta) \end{pmatrix}, \tag{1}$$

where $\mathcal{H}^{l,\chi}(\mathbf{k};\theta)$ is the l-th intralayer Dirac Hamiltonian for valley χ, where $\chi = 1(-1)$ for the $K(K')$-valley, and $\mathbf{k}$ is the moiré-scale crystal momentum. In the continuum model, the Bloch eigenfunctions are expanded in terms of moiré plane waves. Hence, the (N, M)-th block of the l-th intralayer Dirac Hamiltonian is a 2×2 submatrix describing the sublattice coupling as

$$\mathcal{H}_{N,M}^{l,\chi}(\mathbf{k};\theta) = \begin{pmatrix} 0 & h^{l,\chi}(\mathbf{k} + \mathbf{G}_{N,M};\theta) \\ h^{l,\chi}(\mathbf{k} + \mathbf{G}_{N,M};\theta) & 0 \end{pmatrix}, \tag{2}$$

where $\mathbf{G}_{N,M}$ is a moiré reciprocal lattice vector given by $\mathbf{G}_{N,M} = N\mathbf{G}_1 + M\mathbf{G}_2$, with $\mathbf{G}_1 = 2\pi/L(1/\sqrt{3}, 1)$ and $\mathbf{G}_2 = 4\pi/L(-1/\sqrt{3}, 0)$, and $L = a_0/(2\sin(\theta/2)$ is the length of the moiré cell vectors. The integers N, M run over the set $\mathcal{M}$ that indexes moiré reciprocal lattice vectors such that they satisfy

$$\mathcal{M} = \left\{ (N, M) \in \mathbb{Z}^2 \mid \parallel \mathbf{G}_{N,M} \parallel \leqslant p_{\max} \parallel \mathbf{G}_1 \parallel \right\}. \tag{3}$$

Here $p_{\max}$ is an integer controlling the cutoff radius in reciprocal space, and was taken as 5.

The function $h^{l,\chi}(\mathbf{q};\theta)$ is given by

$$h^{l,\chi}(\mathbf{q};\theta) = \chi\hbar v_{\mathrm{F}}(\mathbf{q} - \chi\mathbf{K}_l) \cdot \boldsymbol{\tau}_{\theta}^{l,\chi}, \tag{4}$$

where $\mathbf{K}_l$ is the Dirac point associated with the l-th layer, $v_{\mathrm{F}} = \sqrt{3}ta_0/2\hbar$ is the Fermi velocity in graphene, with t being the hopping amplitude between localized p_z orbitals, and

$$\boldsymbol{\tau}_{\theta}^{l,\chi} = \exp(i\chi\tau_z\theta_l/2)(\tau_x, \chi\tau_y)\exp(-i\chi\tau_z\theta_l/2), \tag{5}$$

with τ_i being the corresponding Pauli matrices, and $\theta_{1,2} = \mp\theta/2$. From now on, we will drop the dependence on θ in the Dirac Hamiltonians, which will be implicitly assumed.

Moving on to the interlayer coupling Hamiltonians, $\mathcal{U}$ [62–64], we have the (N, M)-th submatrix given by

$$\begin{aligned} \mathcal{U}_{N,M}^{\chi} = & U_1^{\chi}\delta^{(2)}(\mathbf{G}_N - \mathbf{G}_M) + \\ & U_2^{\chi}\delta^{(2)}(\mathbf{G}_N - \mathbf{G}_M - \chi\mathbf{G}_1) + \\ & U_3^{\chi}\delta^{(2)}(\mathbf{G}_N - \mathbf{G}_M - \chi(\mathbf{G}_1 + \mathbf{G}_2)), \end{aligned} \tag{6}$$

where $\delta^{(2)}$ is a Kronecker delta function acting in the 2D reciprocal space, with

$$\begin{aligned} U_1^{\chi} &= \begin{pmatrix} u_1 & u_2 \\ u_2 & u_1 \end{pmatrix} \\ U_2^{\chi} &= \begin{pmatrix} u_1 & u_2 e^{-i\frac{2\pi\chi}{3}} \\ u_2 e^{i\frac{2\pi\chi}{3}} & u_1 \end{pmatrix} \\ U_3^{\chi} &= \begin{pmatrix} u_1 & u_2 e^{i\frac{2\pi\chi}{3}} \\ u_2 e^{-i\frac{2\pi\chi}{3}} & u_1 \end{pmatrix}, \end{aligned} \tag{7}$$

acting on the sublattice subspace. The interlayer tunnelings $u_{1,2}$ are taken as $u_1 = 79.7\,\mathrm{meV}$ and $u_2 = 97.5\,\mathrm{meV}$ [63, 66].

For the Hartree electron–electron interactions, we adopt the description proposed by Guinea and Walet [61], where the Hartree Hamiltonian submatrix is given by

$$\mathcal{H}^H = \frac{\delta\rho_G}{\epsilon L}\mathbb{1}. \tag{8}$$

Here $\epsilon = 24$ is the effective dielectric constant describing the external and internal screening [62], and $\delta\rho_G$ is the moiré scale electron density, referenced to charge neutrality, which needs to be self-consistently determined. Note the Hartree interactions treat tBLG to act as 2D sheet, since $\exp(-d|\mathbf{G}|) \approx 1$, where $d \approx 3.35$Å is the interlayer separation, which means this term does not explicitly depend on layer.

Following reference [77], the mean-field Hubbard interactions between electrons due to magnetic ordering are captured by the inter-sublattice coupling Hamiltonian

$$\begin{aligned}\mathcal{H}^{U,l}_{N,M} =& \delta^l_0 \mathcal{S} \delta^{(2)}\left(\mathbf{G}_N - \mathbf{G}_M\right)\\ &+ \delta^l_1 \mathcal{S} \sum_{\mathbf{G}_\star} \delta^{(2)}\left(\mathbf{G}_N - \mathbf{G}_M - \mathbf{G}_\star\right),\end{aligned} \tag{9}$$

where $\mathbf{G}_\star$ represents a reciprocal moiré lattice vector in the first star set $\{\pm\boldsymbol{G}_1, \pm\boldsymbol{G}_2, \pm(\boldsymbol{G}_1 + \boldsymbol{G}_2)\}$, $\mathcal{S}$ is a 2×2 sublattice-coupling matrix describing the magnetic order, the definitions of which are given in Results section 3, and the magnetic order parameters, δ^l_0 and δ^l_1, are determined through

$$\delta^l_0 = 2U\left(n^l_{0,\uparrow} - n^l_{0,\downarrow}\right) \tag{10}$$

and

$$\delta^l_1 = 2U\left(n^l_{G,\uparrow} - n^l_{G,\downarrow}\right), \tag{11}$$

where U is the Hubbard parameter, the factor of 2 accounts for the valley degeneracy, $n^l_{0,\sigma}$ is the constant contribution to the spin-polarized electron density, and $n^l_{G,\sigma}$ is the moiré scale contribution to the spin-polarized electron density. Here we have retained the explicit layer index to be clear that these terms act within a layer.

Incorporating the non-interacting Hamiltonian with the Hartree, $\mathcal{H}^{\mathrm{H}}$, and Hubbard, $\mathcal{H}^U$, contributions, we obtain the valley- and spin-projected continuum Hamiltonian as

$$\mathcal{H}^{\chi,\sigma} = \mathcal{H}^{\mathrm{H}} + (-1)^\sigma \mathcal{H}^U + \mathcal{H}^\chi_0, \tag{12}$$

where $\sigma = 0, 1$ for spin up and down electrons, respectively, and the first two terms are $\propto \mathbb{1}$ in layer space. With the Hamiltonian in equation (12), we solve the eigenvalue equation

$$\mathcal{H}^{\chi,\sigma}(\mathbf{k})\,\mathbf{c}_{\chi,\sigma}(\mathbf{k}) = \mathrm{E}^\chi_\sigma(\mathbf{k})\,\mathbf{c}_{\chi,\sigma}(\mathbf{k}), \tag{13}$$

where $\mathbf{c}_{\chi,\sigma}(\mathbf{k})$ is the eigenvector and $\mathrm{E}^\chi_\sigma(\mathbf{k})$ are the energy eigenvalues for a given spin σ.

The order parameter $\delta\rho_G$ is computed from the eigenstates through

$$\delta\rho_G = \frac{2}{N_k} \sum_{\substack{\sigma,\\ n^{CN}_{\mathrm{occ}}}} \sum_{\substack{\mathbf{k},\mathbf{G}',\\ \mathbf{k}+\mathbf{G}'=\mathbf{q}}} c_{n,\chi,\sigma}(\mathbf{q})\, c^*_{n,\chi,\sigma}(\mathbf{q}+\mathbf{G}), \tag{14}$$

where N_k is the number of k-points sampled in the mini-Brillouin zone, n^{CN}_{occ} denotes the sum of occupied states relative to charge neutrality [61–63, 78], with n being used as short-hand notation in the eigenstate coefficients. Note to include temperature effects, the summation over occupied states is replaced with a summation of the flat bands, still relative to the charge neutrality state, and a Fermi occupation function is included [61–63, 78]. We refrain from further investigating the role of temperature here for simplicity, and focus on the $T = 0$ K limit.

The moiré variation in the spin-polarized electron density $n_{G,\sigma}$ is calculated as

$$n^l_{G,\sigma} = \frac{2}{N_k} \sum_{n_{\mathrm{occ}}} \sum_{\substack{\mathbf{k},\mathbf{G}',\\ \mathbf{k}+\mathbf{G}'=\mathbf{q}}} c^l_{n,\sigma}(\mathbf{q})\, c^{*,l}_{n,\sigma}(\mathbf{q}+\mathbf{G}), \tag{15}$$

and the atomic unit-cell constant spin-polarized density is defined as

$$n^l_{0,\sigma} = \frac{2}{N_k} \sum_{n_{\mathrm{occ}}} \sum_{\substack{\mathbf{k},\mathbf{G}',\\ \mathbf{k}+\mathbf{G}'=\mathbf{q}}} c^l_{n,\sigma}(\mathbf{q})\, c^{*,l}_{n,\sigma}(\mathbf{q}). \tag{16}$$

Note that in calculating these spin densities, all bands below the Fermi level are taken into account, in contrast to the expression for $\delta\rho_G$ in equation (14) where it is relative to charge neutrality in the flat bands, and the factor of 2 in these equations comes from a valley degeneracy. Again, to introduce finite temperature effects, the summation over occupied bands is replaced with a summation over all bands and a Fermi function is introduced.

The order parameters δ_0 , δ_1 , and $\delta\rho_G$ are obtained self-consistently. The convergence criterion was chosen so that the total difference between the successive values of all 3 order parameters is less than 10^{-6}. We note that occasionally the criterion is relaxed for metallic systems. Nonetheless, the order parameters are all converged to at least 3 significant figures.

2.2. Continuum model for tTLG

In the case of tTLG, the external layers are twisted with respect to the central layer by the same angle, resulting in a mirror-symmetric system. The lattice vectors and commensurate integers which describe the system are the same as for tBLG. The spin-valley-projected Hamiltonian for tTLG is similar to that for tBLG, with some slight modifications, and is given by

$$\mathcal{H}_0^{\chi,\sigma}(\mathbf{k}) = \begin{pmatrix} \mathcal{H}^{1,\chi}(\mathbf{k}) & \mathcal{U}^{\chi,\dagger} & \mathbb{0} \\ \mathcal{U}^{\chi} & \mathcal{H}^{2,\chi}(\mathbf{k}) & \mathcal{U}^{\chi} \\ \mathbb{0} & \mathcal{U}^{\chi,\dagger} & \mathcal{H}^{3,\chi}(\mathbf{k}) \end{pmatrix}, \tag{17}$$

where $\mathcal{H}^{3,\chi}(\mathbf{k})$ has the same form as $\mathcal{H}^{1,\chi}(\mathbf{k})$, owing to the mirror symmetry, and $\mathcal{H}^{2,\chi}(\mathbf{k})$ remains unchanged from tBLG.

The Hartree contribution to the Hamiltonian for tTLG is analogous to equation (8), since $\exp(-2d|\mathbf{G}|) \approx 1$. However, as the inner layer is distinct from the outer layers, a crystal field can lower the energy of the middle layer [37], which motivates including $\delta\rho_0^l$. As we only investigate tTLG at charge neutrality here, for simplicity, we neglect the Hartree contribution to the Hamiltonian.

Analogously, the Hubbard Hamiltonian is given by

$$\begin{aligned} \mathcal{H}_{N,M}^{U,l} =& \delta_0^l \mathcal{S} \delta^{(2)}(\mathbf{G}_N - \mathbf{G}_M) \\ &+ \delta_1^l \mathcal{S} \sum_{\mathbf{G}_\star} \delta^{(2)}(\mathbf{G}_N - \mathbf{G}_M - \mathbf{G}_\star). \end{aligned} \tag{18}$$

From the symmetry of tLTG, $\delta_{0/1}^3 = \delta_{0/1}^1 = \delta_{0/1}^o$ and $\delta_{0/1}^2 = \delta_{0/1}^i$ for the other orders, where the superscripts o and i have been introduced to denote outisde and inside layers, respectively. Similar to tBLG, details of the exact form of the magnetic orders will be given in the Results section 3.

Having defined these parameters, the full spin-valley-polarized Hamiltonian of tLTG at charge neutrality, incorporating the non-interacting Hamiltonian and short-ranged Hubbard interactions, is

$$\mathcal{H}^{\chi,\sigma}(\mathbf{k}) = \mathcal{H}_0^{\chi,\sigma} + \mathcal{H}^{U,\sigma}. \tag{19}$$

Obtaining the eigenstates of this Hamiltonian allows us to compute the order parameters, $\delta_0^o, \delta_1^o, \delta_0^i, \delta_1^i$, analogously to the twisted bilayer case. We use the same self-consistency criteria for these calculations.

3. Results

3.1. tBLG

3.1.1. Leading instabilities

The leading magnetic instabilities can be obtained from atomistic RPA calculations at $\mathbf{q} = 0$ [74, 75]. Details of these calculations can be found in the papers by Klebl *et al* [74, 75]. The eigenvectors of these RPA calculations characterize the type and form of these magnetic instabilities, ζ_i. The values of which are proportional to the spin-polarized electron density, $\zeta \propto n_\uparrow - n_\downarrow$, where n_σ is the electron density of spin σ. The FM order, moiré modulated antiferromagnetic (MAFM), and nodal antiferromagnetic (NAFM) orders were found to be the most prevalent in magic-angle tBLG [74, 75], which can be seen in figure 1.

As seen in figure 1, and discussed in [74, 75], the FM order is characterized by a spin-polarized electron density peaked in the AA regions of the moiré unit cell. This FM order approximately follows a cosine series with the first reciprocal lattice vectors and a constant shift. As the AA region is centered at the origin, we can approximate the FM order by

$$\zeta_{\mathrm{FM}} = \zeta_0 + \zeta_1 \sum_i \cos(\mathbf{G}_i \mathbf{r}), \tag{20}$$

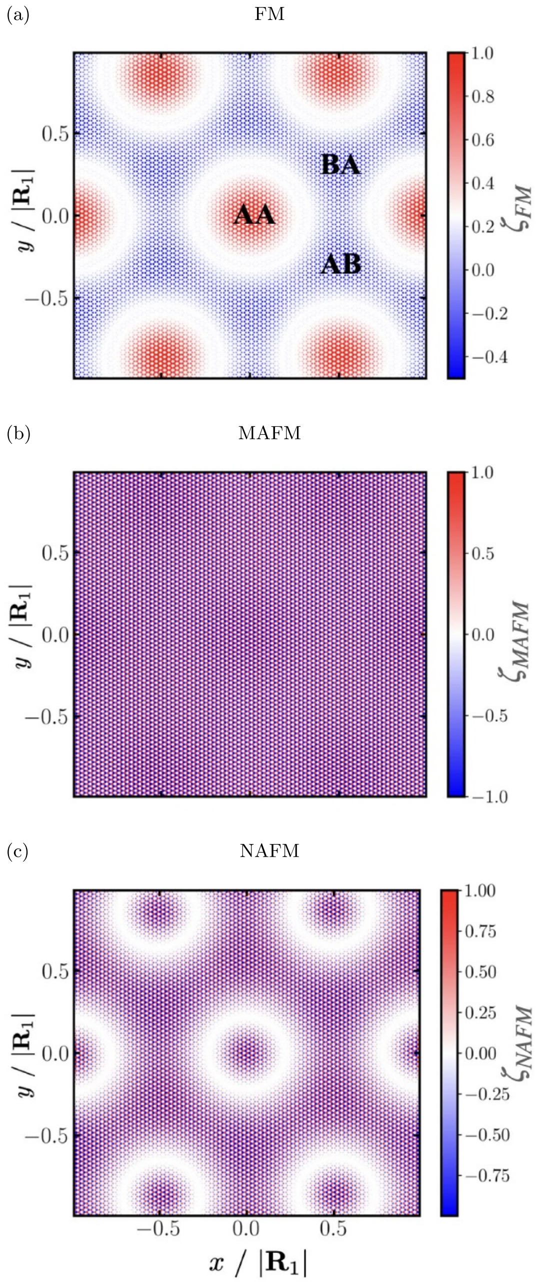

Figure 1. Magnetic instabilities obtained from atomistic RPA calculations. The ferromagnetic order (FM), moiré modulated antiferromagnetic (MAFM), and nodal antiferromagnetic (NAFM) orders are shown in (a)–(c), respectively. Note these graphs are obtained from the eigenvectors of these RPA calculations, corresponding to the most negative eigenvalues, where the largest positive value was chosen to be 1.

where $\boldsymbol{G}_i$ are the moiré reciprocal lattice vectors ($\boldsymbol{G}_1$, $\boldsymbol{G}_2$, and $\mathbf{G}_1 + \mathbf{G}_2$), ζ_0 is a parameter which characterizes the constant contribution spin-polarized electron density in the moiré unit cell, and ζ_1 represents the moiré-scale modulation of the FM order. Since for the FM instability the sublattice polarization is the same, the sublattice-coupling matrix $\mathcal{S}$ is taken to be the 2×2 identity matrix in the sublattice space.

For the MAFM order, there is a similar moiré scale spin structure, but the value of ζ changes sign between each sublattice, implying $\mathcal{S} \propto \sigma_z$. Therefore, the MAFM order can also be approximately characterized by

$$\zeta_{\mathrm{MAFM}} = \zeta_0 + \zeta_1 \sum_i \cos\left(\mathbf{G}_i \mathbf{r}\right), \tag{21}$$

where ζ_0 and ζ_1 have opposite sign for each sublattice, but the same sign within each sublattice on different layers.

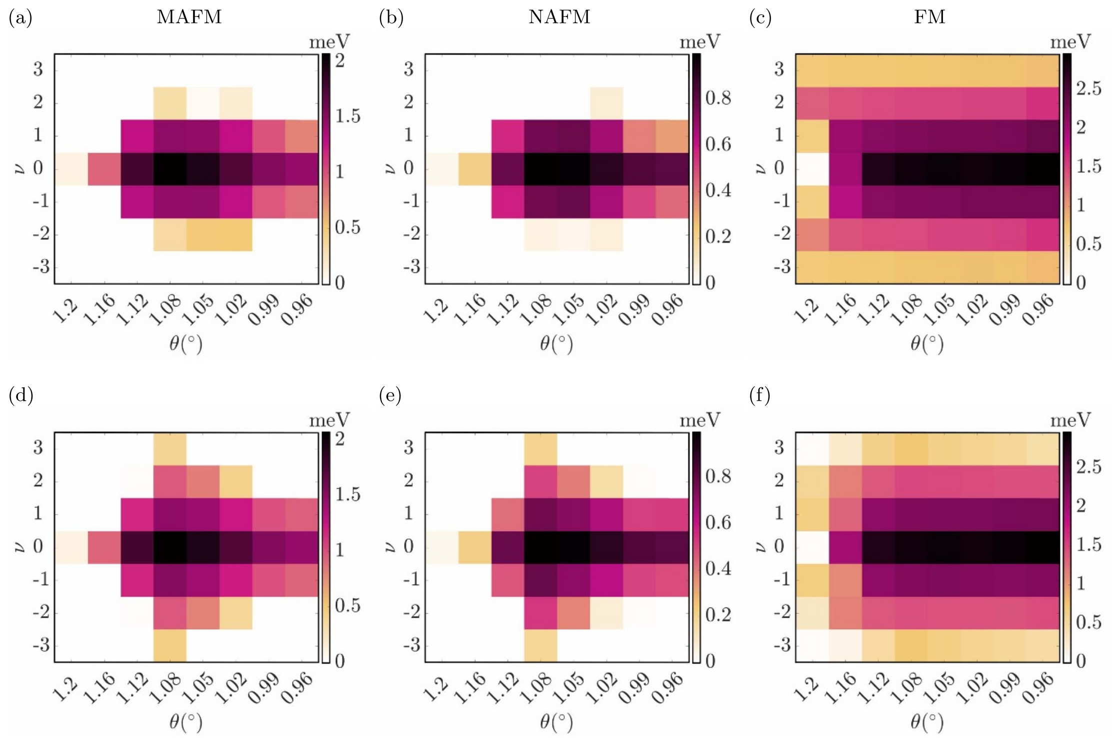

Figure 2. Magnitudes of Hubbard potential order parameters $|\delta_0| + |\delta_1|$, for the considered instabilities , to establish where these phases can exist at twist angle (θ) close to the magic angle and for integer doping levels within the flat bands (ν). With Hartree interactions, we show results for MAFM in (a), NAFM in (b), and FM in (c). Results without Hartree interactions are shown in (d) for MAFM, (e) for NAFM, and (d) for FM. $U = 2\,\text{meV}$ throughout. We note that $\delta_0 = 0$ for the NAFM order.

Finally, the NAFM is analogous to the MAFM case, but without a constant-shift term, which means it can be approximated as

$$\zeta_{\text{NAFM}} = \zeta_1 \sum_i \cos\left(\mathbf{G}_i \mathbf{r}\right). \tag{22}$$

Again ζ_1 has the opposite sign for each sublattice, meaning $\mathcal{S} \propto \sigma_z$.

3.1.2. Regions of stability

We included these leading magnetic instabilities in the continuum model and solved the resulting Hamiltonian self-consistently (see section 2). To perform these calculations, we need to choose a value of the on-site Hubbard parameter in the continuum model. In the atomistic model, the value of U_z for p_z orbitals is known to be $\sim$10 eV [79, 80], which can be approximated by $U_z \approx \mathrm{e}^2/4\pi\epsilon a_0$ [61]. Following Guinea and Walet [61], these p_z values need to be projected onto the moiré wavefunctions, which gives the moiré Hubbard parameter to be $U \approx (U_z N^{-2})N \approx \mathrm{e}^2 a_0/4\pi\epsilon L^2$, where $N \approx (L/a_0)^2$ is the number of atoms in the moiré unit cell. Since the lattice parameter of graphene is $\sim$2 Å and the moiré scale is $\sim$100 Å, the value of $U \sim 1$ meV. In comparison, the Hartree interaction is L/a_0 larger, which dominates over the Hubbard interaction, which motivated neglecting the Hubbard interaction term previously [61]. However, an energy scale of $\sim$1 meV is still similar to the bandwidth of tBLG at the magic angle, which means these interactions can still be important [77]. In this section, we choose $U = 2$ meV to solve our system of equations self-consistently, which is comparable to the values used by Jimeno-Pozo *et al* [77].

To quantify the stability of the magnetic orders, the magnitudes of order parameters $|\delta_0| + |\delta_1|$ are displayed in figure 2 as a function of doping level (ν) and twist angle (θ), with and without long-range Coulomb interactions. The cutoff for considering a magnetic order as stable is set at $|\delta_0| + |\delta_1| \leqslant 5 \times 10^{-2}$ meV, below which the Hubbard potentials are too weak to induce any observable modifications to the band structures.

In figure 2(a) we show results for the total order parameter ($|\delta_0| + |\delta_1|$) of MAFM, which indicates if this magnetic order survives at the considered twist angle and doping level, with account of Hartree interactions. The MAFM magnetic order strongly persists from $\theta = 1.12°$ to $\theta = 0.96°$ inside the doping range of $\nu = \pm 1$. Notably, the symmetry broken state is most strongly stabilized near charge neutrality at the magic angle $\theta = 1.08°$, with a total order parameter of 2.1 meV, away from which the order parameters are suppressed. Upon doping in the range of $\theta = 1.08° - 1.02\ °$, stable MAFM order persists up to $\nu = \pm 2$, albeit being reduced by an order of magnitude to $\sim$0.1 meV at $\nu = \pm 2$ for $\theta = 1.08° - 1.02\ °$. For twist angles outside of this window the order parameter decays more rapidly as the system is doped, i.e. more doping levels near the magic angle host magnetic order, while the twist angles further from the magic angle only host magnetic order near charge neutrality.

The order parameter for NAFM with Hartree interactions, as shown in figure 2(b), exhibits similar trends as function of the twist angle and doping as the MAFM case. The magnitude of the order parameter for NAFM relative to MAFM is reduced by approximately 1/2 because NAFM order does not have δ_0. Similar to MAFM, NAFM is most stable near charge neutrality at the magic angle, with it strongly decaying in the doping variable, hardly existing outside of $\nu = \pm 1$, but weakly decaying with twist angle away from the magic angle.

The FM order with Hartree interactions, shown in figure 2(c), is most stable at charge neutrality, with a total order parameter around 3 meV near the magic angle. The FM order is also suppressed upon doping the system, while being relatively constant over twist angles near the magic angle. Upon twisting to larger angles, the magnetic order is suppressed at charge neutrality first. At $\theta = 1.2°$, the FM order is suppressed at charge neutrality, but stable FM orders persist near $\nu = \pm 2$, with a total order parameter amplitude of around 1.5 meV. The $\theta = 1.2°$ twist angle is the only one we observed to have a non-monotonic doping dependence of the FM, whereas for all other angles the FM order parameter decays monotonically from charge neutrality. At smaller angles than those considered here, it is expected the FM is again destabilized first at charge neutrality.

The effect of long-ranged interactions is also investigated by considering the value of the magnetic order parameter when the Hartree interactions are not taken into account. In other words, we consider the stability of the magnetic order for different twist angles and doping levels when only short-ranged Hubbard interactions are present. The phase diagrams for these calculations are shown in figures 2(d)–(f).

The anitferromagnetic (AFM), MAFM (figure 2(d)) and NAFM (figure 2(e)) orders, have clear differences in the absence of Hartree interactions. The phase diagrams are slightly more electron–hole symmetric compared to when Hartree interactions are taken into account. Furthermore, the magnetic order parameter exists over a wider range of doping levels, and is significant at $\nu = \pm 3$ for the magic angle $\theta = 1.08°$. Otherwise, the qualitative variations remain similar at other twist angles and dopings compared to when long-range Coulomb interactions are taken into account. We do not notice any large differences in the magnitudes of the order parameters between these cases.

For the FM order without Hartree interactions, as shown in figure 2(f), the qualitative variation and magnitude of the order parameters are similar to that in the presence of Hartree interaction. However, the reduction of the order parameters is more rapid with doping levels away from charge neutrality, in contrast to when Hartree interactions are taken into account. For example, at $\theta = 1.16°$, although the stable orders are still centered around charge neutrality, the magnitude at $\nu = \pm 3$ is significantly reduced. Moreover, at $\theta = 1.2°$, FM order is only stable at $\nu = \pm 1$ and ± 2.

Overall, comparing figures 2(a), (b), (d) and (e), we find that the AFM orders are enhanced by the long-ranged Hartree interactions at $\nu = \pm 1$ near the magic angle. Beyond this doping level, Hartree interactions suppress AFM order. On the contrary, comparing figures 2(c) and (f), the FM order is always enhanced by Hartree interactions. Such differences lie in the interplay between short and long-ranged interactions, which also underpins the distortions of the band structures.

3.1.3. Band structure

The advantage of the approach developed here, unlike the atomistic RPA approach [74] and the perturbative continuum approach [77], is that self-consistent quasi-particle band structures can also be investigated. In this section, we report these for magic-angle tBLG for the leading instabilities, as a function of doping with the inclusion of long-range Hartree interactions, as seen in figure 3. We restrict our analysis here to only electron-doped systems, as hole-doping is qualitatively similar (albeit with band distortions in the opposite direction of energy) [81]. Moreover, we use a value of $U = 4$ meV to stabilize the magnetic orders at all doping levels to make it more clear how gaps at high symmetry points vary with doping level, as summarized in table 1. In the supporting information we show additional results for the band structures with $U = 2$ meV, with their band gaps also being reported in table 1.

The band structures without magnetic order but with Hartree interactions (note that when Hartree interactions are not taken into account, the $\nu = 0$ band structure applies for all doping levels, as the Hartree interactions in the model at charge neutrality vanish) are shown in figure 3(a) for reference. As electrons are added into the normal state of tBLG, this causes the K-points to increase in energy

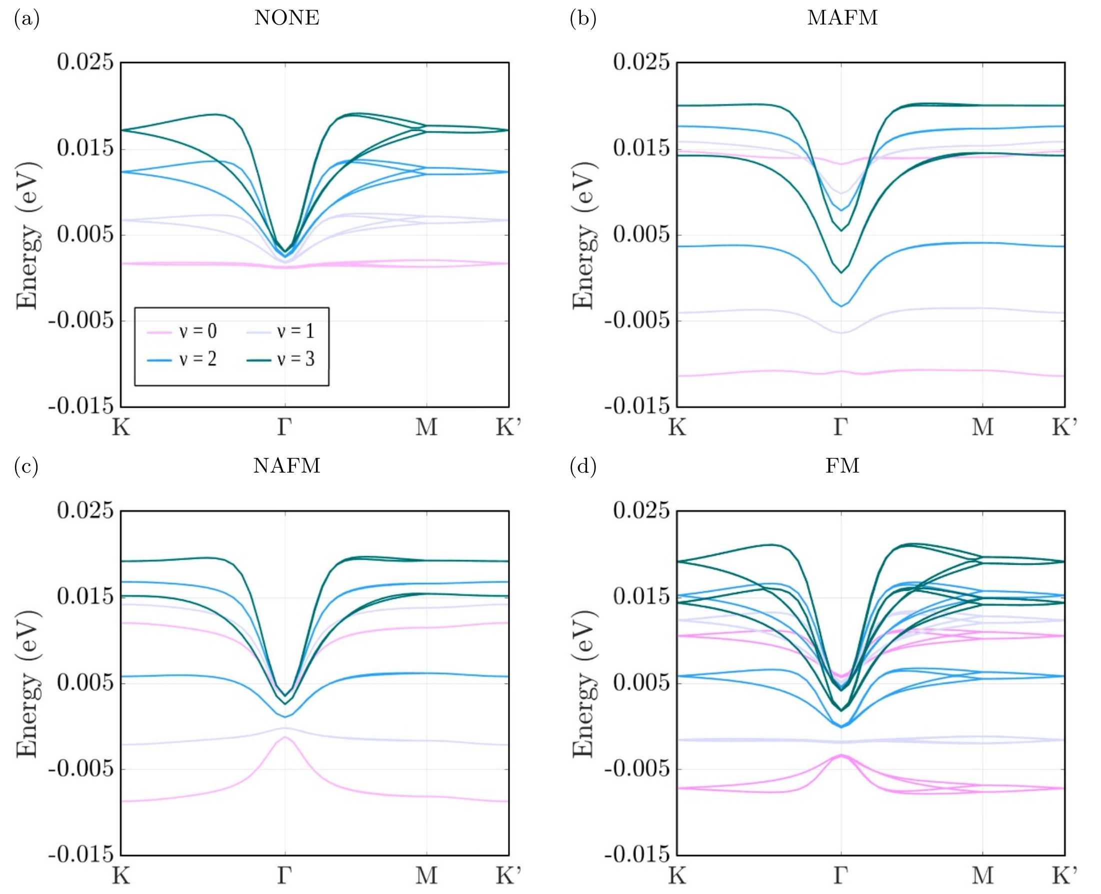

Figure 3. The self-consistent band structures at 1.08° for different fillings ν for (a): Hartree corrections only, (b): MAFM, (c): NAFM, and (d): FM. We note that a large Hubbard parameter ($U = 4$ meV) was chosen to demonstrate the effects of gap opening on Hartree-corrected bands. Color represents different filling factors: light pink for $\nu = 0$; light blue for $\nu = 1$; blue for $\nu = 2$ and dark green for $\nu = 3$.

Table 1. Values of the band gaps, in units of meV, at K/K' points for the AFM magnetic order (MAFM and NAFM), and values between the spin-split K/K' points of the FM order. These are shown for different values of U, in units of meV, and for the indicated doping levels at the studied twist angle of 1.08°.

U	Order	$\nu = 0$	$\nu = 1$	$\nu = 2$	$\nu = 3$
4	**FM**	18	14	9	5
	MAFM	26	20	14	6
	NAFM	21	16	11	4
2	**FM**	9	7	5	2
	MAFM	4	4	1	0
	NAFM	4	3	0	0

relative to the Γ-points, causing a sensitive dependence of the band structure on doping, and a pinning of the van Hove singularities. At the magic angle, this causes the bands to become more dispersive, but at other twist angles these distortions cause doping-induced band flattening, in addition to the twist-angle induced band flattening. A detailed analysis of the band distortions induced by Hartree interaction is presented in [62, 63, 81, 82].

The band structures for the MAFM and NAFM magnetic orders are shown in figures 3(b) and (c), respectively. For both of these magnetic orders, a large gap is created at the K/K' points, owing to the sublattice symmetry breaking. For the charge neutral cases, the electronic bands are extremely flat over most of the Brillouin zone, and the system is a narrow-gap insulator. The effect of Hartree interactions with doping causes the bands at the edge of the Brillouin zone to distort to higher energies, as was the case without magnetic order. For the other doping levels, the system becomes a metal, owing to partially filled dispersive bands. In each case, however, there remains a significant gap at the K/K' point, albeit decreasing with increasing doping level away from charge neutrality, with $\nu = 3$ only having a small gap. In table 1 we report the values of the gaps at the K/K' points for these magnetic orders.

The band structures for the FM order are shown in figure 3(d). At each doping level there exist two sets of bands around the Fermi energy, which can be attributed to the spin-polarization of the electronic states, but the valley symmetry is not broken. At charge neutrality, one set of these bands is pushed lower in energy and the other set of bands are pushed to higher energies. Overall, at charge neutrality, a gap exists at the Fermi energy, which means the system is a FM insulator. In addition to the spin-splitting of the bands, which occurs because of the constant term in the order parameter, within each spin-polarized band there are significant distortions to the electronic structure analogous to Hartree distortions. For the spin state that is lowered in energy, the electronic states at the edge of the Brillouin zone are lower in energy than the states near the Γ point. While for the band of the spin state that is higher in energy, the electronic states at the edge of the Brillouin zone are raised with respect to the Γ point. Therefore, opposite distortions occur for each spin state. Moreover, while these distortions are analogous to the distortions from Hartree interactions upon doping, the opposite trends occur. Specifically, for the completely filled spin band, the Hubbard interactions cause the states at the edge of the Brillouin zone to lower energies, while Hartree interactions for a completely filled band push these states higher in energy. Therefore, the distortions from FM Hubbard and Hartree interactions compete, with Hartree interactions dominating at larger doping levels.

For the other doping levels, the system to become an FM metal instead of an insulator, as there is overlap of the spin-polarized bands or/and partially filled bands. With increasing doping level, we know that the FM state monotonically weakens, see figure 3. This can clearly be seen from the shrinking energy separation of the spin-split Dirac cones at K/K'. In table 1 we also report the gaps between the spin-split Dirac cones at the K/K' points.

3.2. tTLG

3.2.1. Leading instabilities

We now turn our attention to the mirror-symmetric tTLG. This system also exhibits a magic angle, but at a twist angle of $|\theta| = 1.54^\circ$ [37]. For tTLG, we follow the same procedure for our calculations as tBLG [37]. First we found the leading instabilities from the RPA calculations, inspected these magnetic instabilities (only some of which are shown in figure 4), constructed appropriate approximate forms for the order parameters and performed self-consistent continuum Hartree+U calculations.

Similarly to tBLG, we find a FM order in tTLG. As the inside and outside layer(s) of tTLG are not equivalent, we show an outside layer in figure 4(a) and the inside layer in figure 4(c). We find the FM order is peaked mainly on the AAA regions of the inner layer [37]. Analogously to the bilayer, we can approximate this magnetic order with the form

$$\zeta_{\mathrm{FM}}^{(j)} = \zeta_0^{(j)} + \zeta_1^{(j)} \sum_i \cos\left(\mathbf{G}_i \mathbf{r}\right), \tag{23}$$

where (j) is now a layer index (either o or i), as the order parameters can now vary between the layers. From the symmetry of the structure, the outside layers are equivalent, so we only need to consider the parameters to be distinct for outside vs. inside. Therefore, there are only four parameters for this magnetic order. The direction of such polarization is the same on the different sublattices, meaning that the sublattice-coupling $\mathcal{S}$ is taken to be the identity matrix for each layer.

Another candidate order is the MAFM/MAFM (MMAFM) magnetic order, where both the outer and inner layers are in a moiré-scale MAFM, as seen in figures 4(b) and (d) for the outer and inner layers, respectively. This can be characterized by the following form

$$\zeta_{\mathrm{MMAFM}}^{(j)} = \zeta_0^{(j)} + \zeta_1^{(j)} \sum_i \cos\left(\mathbf{G}_i \mathbf{r}\right). \tag{24}$$

In this case, the spin polarization in each layer is identical, and similarly to the MAFM case for tBLG, there is an opposite sign for each sublattice, meaning that $\mathcal{S}$ is taken as the Pauli matrix σ_z .

With the magnetic orders from the atomistic RPA transcribed into the continuum description, we solved for the magnetic orders self-consistently and obtained the band structures self-consistently at the magic angle of 1.54 in tTLG. Further details of how these magnetic orders are included in the Hamiltonian are given in the methods section 2. Note we do not construct a full phase diagram for tTLG, as we did for tBLG, since a full RPA phase diagram for tTLG has not been computed yet. Moreover, the magnetic orders of tTLG can be a lot more varied than tBLG, but we only choose to study two here as a representative case to demonstrate our method can easily be extended to other moiré graphene multilayers.

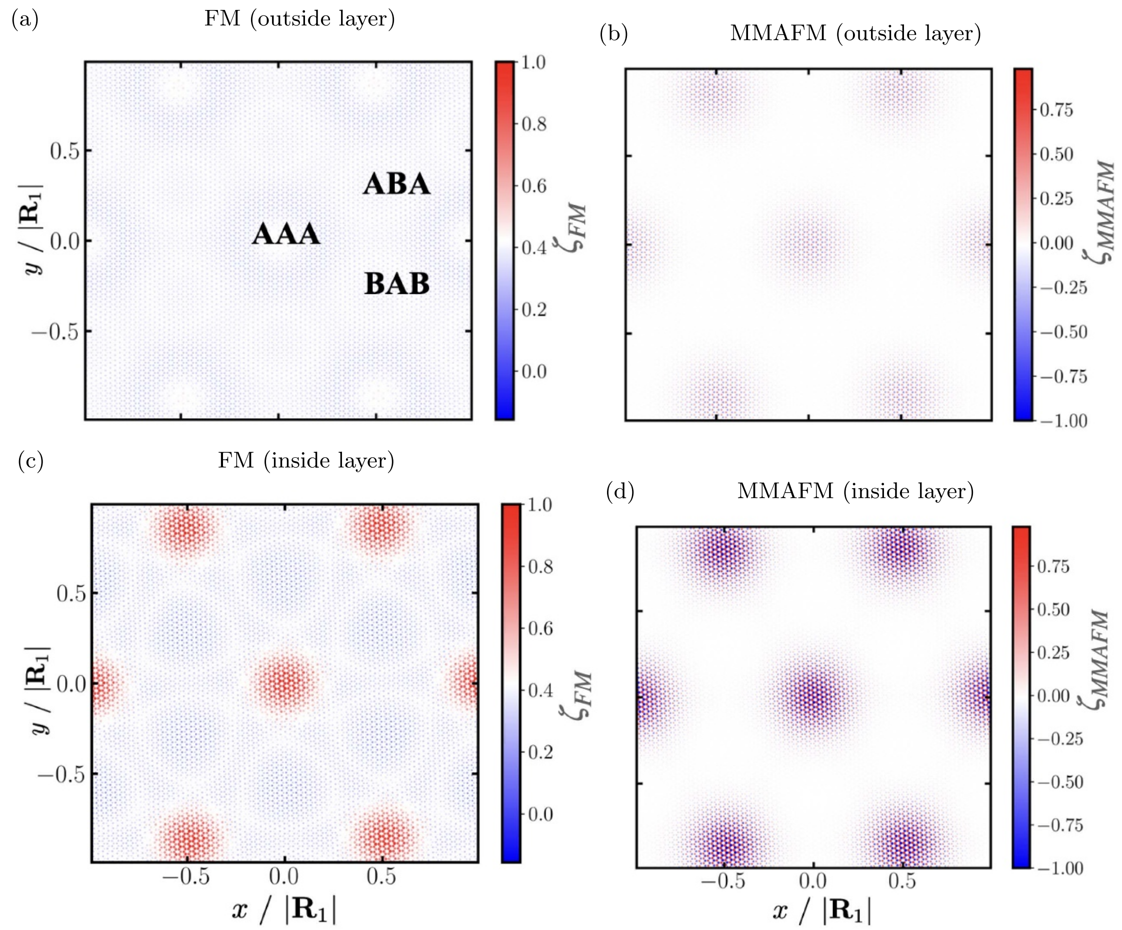

Figure 4. Magnetic instabilities obtained from atomistic RPA calculations. Here we only consider the ferromagnetic order (FM) and MAFM/MAFM (MMAFM) order. Since the outside and insider layers are inequivalent, we show them separately, and since the outside layers are equivalent we only show one of them. The outside and inside layers of FM are shown in (a) and (c), respectively, while the outside and inside layers of MMAFM are respectively in (b) and (d). Note these plots are from the eigenvectors of the RPA calculations, where the largest value was chosen to be ±1. These values are proportional to the spin-polarized electron density.

3.2.2. Band structures

In figure 5 the normal state band structure is shown in orange for reference. The band structure of tTLG is analogous to tBLG, but where there is an additional set of Dirac cones with large Fermi velocities compared to the flat bands, and the magic-angle of the flat bands is $\sqrt{2}$ times larger than tBLG. As we are studying tTLG at charge neutrality, Hartree interactions can be neglected.

The band structure of the FM state of magic angle tTLG is shown in figure 5(a). We found that this order can be stabilized with a Hubbard parameter of $U = 1$ meV at charge neutrality. The pair of valence and conduction flat bands in the normal state are each split into a pair of spin-polarized bands, giving rise to four valley-degenerate flat bands in this magnetic order, similar to the observations in tBLG. The splitting between the spin-polarized valence flat bandsis around 1 meV at the Γ-point and around 2 meV at the M-point. At the $K(K')$-points, there is a band gap of around 3.1 meV in the flat bands due to time-reversal symmetry breaking in this order (although this symmetry breaking is not large enough to lift the degeneracy of the Dirac cone with the large Fermi velocity).

By raising the Hubbard parameter to $U = 2$ meV, the MMAFM order can also be stabilized, which is shown in figure 5(b). There is spin and valley degeneracy of bands, while a band gap at the K-point of around 0.93 meV persists. It does not, however, change the size of the band gaps at the Γ- and M-points. We found that these gaps further open for $U > 3$ meV.

It is worth noting that, for both the FM and MMAFM orders, the graphene-like Dirac cones, i.e. those with a large Fermi velocity, remain unperturbed and do not hybridize with the flat bands. In general, for the FM and MMAFM orders, which can be stabilized with a relatively small U, the magnitude of the order parameters are around 0.1 meV. For the FM order, the constant background (δ_0) in all layers is approximately twice the strength of the moiré-scale (δ_1) oscillations. However, in the MMAFM order, the strengths of the constant (δ_0) and moiré (δ_1) part are almost equal in each of the

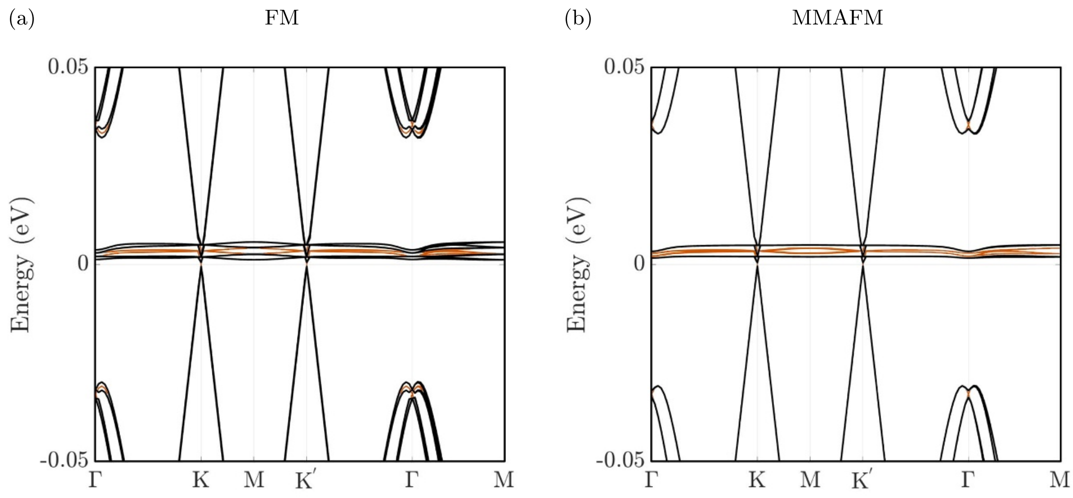

Figure 5. Self-consistent band structures obtained of tTLG at charge neutrality at $\theta = 1.54°$ for (a) FM and (b) MMAFM. The band structure at charge neutrality without any Hubbard interactions is included in orange.

layers. It is also found that the inner layer exhibits a stronger polarization than the outer layers, possibly because of the 'doubled' moiré superlattice formed with the two outer layers, which enhances the moiré electronic effects specifically for the inner layer.

4. Discussion and conclusions

The self-consistent band structures we have obtained are consistent with those from Jimeno-Pozo *et al* [77] and Klebl *et al* [74, 75], who performed non-self-consistent calculations of tBLG. For example, the AFM orders which break sublattice symmetry of the graphene layers cause the a gap to open in the Dirac cones, creating an insulating state at charge neutrality. Previously, however, the FM order was not investigated. The FM order does not break the sublattice symmetry, but it does break the spin degeneracy, causing the bands to spin-split, creating an insulating state at charge neutrality for tBLG for large enough values of U. Overall, the self-consistent electronic structures obtained here qualitatively agree with those from Jimeno-Pozo *et al* [77] and Klebl *et al* [74, 75], and moreover, we have extended them to FM order and tTLG.

By inspecting the regions of stability of the three competing ground state magnetic orders, there are also a number of notable similarities to the RPA predictions performed by Klebl *et al* in reference [75]. According to the RPA calculations carried out in reference [74], the critical values of Hubbard parameter U_C reach a minimum near $\theta = 1.08° - 1.05°$ both with Hartree and without Hartree interactions. This indicates that tBLG is susceptible to magnetic symmetry broken phases near the magic angle. Our predicted region of stability for MAFM and NAFM is consistent with this picture, in that the largest order parameters are found near the magic angle and decay away from it. Furthermore, in the RPA calculations it was found that FM order tends to occur at the critical U_C for doped systems instead of $M(N)$AFM order, which becomes more pronounced with Hartree interactions. Using the continuum model in this work we also find that the $M(N)$AFM order parameters are suppressed for larger doping levels, but find the FM order can persist and is enhanced by Hartree interactions. Therefore, overall the self-consistent diagrams obtained here are qualitatively consistent with those by Klebl *et al* [75].

In the context of experimental measurements, our calculations reproduce some of the observed states, but not all of them. For tBLG, we predict a correlated insulating state at charge neutrality from AFM order, owing to the sublattice symmetry breaking lifting the Dirac point, and also potentially an insulating state from FM order. In experiments, we are not aware of any reports of a FM state at charge neutrality, but the correlated insulating states observed at charge neutrality could have AFM order [5, 18, 26, 28, 34]. In the context of tTLG, the conclusion is similar, which agrees with experiments at charge neutrality [36]. While our model has the pinning of van Hove singularities from Hartree interactions upon doping, we do not predict any other insulating states at other doping levels, for both tBLG [3, 11, 14] and tTLG. In contrast, experiments of tBLG and tTLG, which have correlated insulating states observed at practically all integer doping levels in the flat moiré bands [5]. Therefore, agreement with experiments is partial, which motivates further development of our approach.

As the assumed magnetic orderings here do not break valley symmetries, creating insulating states at doping levels other than charge neutrality is not possible with the interactions included here. To go beyond this limtation, we must include longer-ranged exchange (Fock, for example) interactions, or modify the expression for the magnetic order parameters. For example, in tBLG we have constrained the magnetic orders to be a sum of cosines with certain polarization on each sublattice, sometimes also including a sublattice polarized constant contribution. Instead, we could allow, for example, the sublattice polarization to be different in the constant and cosine contributions, allowing for more complex magnetic orderings. In the trilayer, many more instabilities were observed from the RPA calculations, and these could be included, or again more general forms of the magnetic instabilities included and self-consistently solved to find a ground state.

Overall, we have presented a formalism for the self-consistent inclusion of atomic-scale Hubbard interactions into the continuum model of moiré graphene multilayers. We have investigated this for tBLG and tTLG, for a number of magnetic instabilities, twist angles and doping levels. These developments can be used to investigate the interplay between long-ranged and short-ranged exchange interactions, and also magnetic order in other moiré graphene multilayers, such as tDBLG.

Data availability statement

The data that support the findings of this study are openly available at the following URL/DOI: https://github.com/VVitale/TBLG-U [83].

Supplementary Materials available at https://doi.org/10.1088/1361-6528/ae2d5e/data1.

Acknowledgments

We thank A Jimeno-Pozo and F Guinea for helpful discussions. C T S C acknowledges funding from the Croucher Foundation and an Imperial College President's Scholarship. Z A H G acknowledges support through the Glasstone Research Fellowship in Materials, University of Oxford. We acknowledge the Thomas Young Centre under Grant No. TYC-101. AF and DMK acknowledge funding by the DFG within the Priority Program SPP 2244 '2DMP' – 443274199. V. V. acknowledges support from the European Union NextGenerationEU—M4, C2, Investment line 1.2 - title "Ultrafast exciton dynamics and optoelectronics in moiré superlattices—UltraDYNOMOS", CUP N. B53C24010860005. This project has received funding from the European Union's Horizon 2020 research and innovation programme under the Marie Sklodowska-Curie Grant Agreement No. 101067977.

Author contributions

Christopher T S Cheung
Investigation (lead), Visualization (equal), Writing – original draft (equal)

Valerio Vitale 0000-0003-2714-8585
Conceptualization (equal), Investigation (equal), Methodology (equal), Software (equal), Supervision (equal), Visualization (equal), Writing – original draft (equal), Writing – review & editing (equal)

Lennart Klebl 0000-0002-5453-9779
Conceptualization (equal), Data curation (equal), Investigation (equal), Methodology (equal), Software (equal), Writing – review & editing (equal)

Ammon Fischer
Conceptualization (equal), Investigation (equal), Software (equal), Writing – review & editing (equal)

Dante M Kennes
Funding acquisition (equal), Supervision (equal), Writing – review & editing (equal)

Arash A Mostofi 0000-0002-6883-8278
Funding acquisition (equal), Supervision (equal)

Johannes Lischner
Conceptualization (equal), Funding acquisition (equal), Supervision (equal), Writing – review & editing (equal)

Zachary A H Goodwin 0000-0003-2760-4499
Conceptualization (equal), Investigation (equal), Methodology (equal), Software (equal), Supervision (equal), Visualization (equal), Writing – original draft (equal), Writing – review & editing (equal)

References

[1] Cao Y *et al* 2018 *Nature* **556** 80
[2] Cao Y, Fatemi V, Fang S, Watanabe K, Taniguchi T, Kaxiras E and Jarillo-Herrero P 2018 *Nature* **556** 43
[3] Jiang Y, Lai X, Watanabe K, Taniguchi T, Haule K, Mao J and Andrei E Y 2019 *Nature* **573** 91
[4] Sharpe A L, Fox E J, Barnard A W, Finney J, Watanabe K, Taniguchi T, Kastner M A and Goldhaber-Gordon D 2019 *Science* **365** 605
[5] Lu X *et al* 2019 *Nature* **574** 653
[6] Cao Y, Luo J Y, Fatemi V, Fang S, Sanchez-Yamagishi J D, Watanabe K, Taniguchi T, Kaxiras E and Jarillo-Herrero P 2016 *Phys. Rev. Lett.* **117** 116804
[7] Carr S, Massatt D, Fang S, Cazeaux P, Luskin M and Kaxiras E 2017 *Phys. Rev. B* **95** 075420
[8] Zou L, Po H C, Vishwanath A and Senthil T 2018 *Phys. Rev. B* **98** 085435
[9] Choi Y *et al* 2019 *Nat. Phys.* **15** 1174
[10] Kang J and Vafek O 2019 *Phys. Rev. Lett.* **122** 246401
[11] Kerelsky A *et al* 2019 *Nature* **572** 95
[12] Lucignano P, Alfé D, Cataudella V, Ninno D and Cantele G 2019 *Phys. Rev. B* **99** 195419
[13] Polshyn H, Yankowitz M, Chen S, Zhang Y, Watanabe K, Taniguchi T, Dean C R and Young A F 2019 *Nat. Phys.* **15** 1011
[14] Xie Y, Lian B, Jäck B, Liu X, Chiu C L, Watanabe K, Taniguchi T, Bernevig B A and Yazdani A 2019 *Nature* **572** 101
[15] Yankowitz M, Chen S, Polshyn H, Zhang Y, Watanabe K, Taniguchi T, Graf D, Young A F and Dean C R 2019 *Science* **363** 1059
[16] Yoo H *et al* 2019 *Nat. Mater.* **18** 448
[17] Andrei E Y and MacDonald A H 2020 *Nat. Mater.* **19** 1265
[18] Cao Y, Chowdhury D, Rodan-Legrain D, Rubies-Bigorda O, Watanabe K, Taniguchi T, Senthil T and Jarillo-Herrero P 2020 *Phys. Rev. Lett.* **124** 076801
[19] Carr S, Fang S and Kaxiras E 2020 *Nat. Rev. Mater.* **5** 748
[20] Balents L, Dean C R, Efetov D K and Young A F 2020 *Nat. Phys.* **16** 725
[21] Bultinck N, Khalaf E, Liu S, Chatterjee S, Vishwanath A and Zaletel M P 2020 *Phys. Rev. X* **10** 031034
[22] Nuckolls K P, Oh M, Wong D, Lian B, Watanabe K, Taniguchi T, Bernevig B A and Yazdani A 2020 *Nature* **588** 610
[23] Xie M and Macdonald A H 2020 *Phys. Rev. Lett.* **124** 097601
[24] Zhang Y, Jiang K, Wang Z and Zhang F 2020 *Phys. Rev. B* **102** 035136
[25] Zondiner U *et al* 2020 *Nature* **582** 203
[26] Cao Y, Rodan-Legrain D, Park J M, Yuan N F Q, Watanabe K, Taniguchi T, Fernandes R M, Fu L and Jarillo-Herrero P 2021 *Science* **372** 264
[27] Choi Y *et al* 2021 *Nat. Phys.* **17** 1375
[28] Das I, Lu X, Herzog-Arbeitman J, Song Z D, Watanabe K, Taniguchi T, Bernevig B A and Efetov D K 2021 *Nat. Phys.* **17** 710
[29] Liu J and Dai X 2021 *Phys. Rev. B* **103** 035427
[30] Kennes D M, Claassen M, Xian L, Georges A, Millis A J, Hone J, Dean C R, Basov D N, Pasupathy A N and Rubio A 2021 *Nat. Phys.* **17** 155
[31] Rozen A *et al* 2021 *Nature* **592** 214
[32] Saito Y, Yang F, Ge J, Liu X, Taniguchi T, Watanabe K, Li J I, Berg E and Young A F 2021 *Nature* **592** 220
[33] Oh M, Nuckolls K P, Wong D, Lee R L, Liu X, Watanabe K, Taniguchi T and Yazdani A 2021 *Nature* **600** 240
[34] Wu S, Zhang Z, Watanabe K, Taniguchi T and Andrei E Y 2021 *Nat. Mater.* **20** 488
[35] Xie Y *et al* 2021 *Nature* **600** 439
[36] Hao Z, Zimmerman A M, Ledwith P, Khalaf E, Najafabadi D H, Watanabe K, Taniguchi T, Vishwanath A and Kim P 2021 *Science* **371** 1133
[37] Fischer A, Goodwin Z A H, Mostofi A A, Lischner J, Kennes D M and Klebl L 2022 *npj Quantum Mater.* **7** 1
[38] Zhang C *et al* 2021 *Nat. Commun.* **12** 2516
[39] Rubio-Verdú C *et al* 2021 *Nat. Phys.* **18** 196–202
[40] He M, Li Y, Cai J, Liu Y, Watanabe K, Taniguchi T, Xu X and Yankowitz M 2021 *Nat. Phys.* **17** 26–30
[41] Liu X *et al* 2020 *Nature* **583** 221
[42] Goodwin Z A H, Klebl L, Vitale V, Liang X, Gogtay V, van Gorp X, Kennes D M, Mostofi A A and Lischner J 2021 *Phys. Rev. Mater.* **5** 084008
[43] Seiler A M, Geisenhof F R, Winterer F, Watanabe K, Taniguchi T, Xu T, Zhang F and Weitz R T 2022 *Nature* **608** 298
[44] Zhou H, Xie T, Taniguchi T, Watanabe K and Young A F 2021 *Nature* **598** 434
[45] Zhou H, Holleis L, Saito Y, Cohen L, Huynh W, Patterson C L, Yang F, Taniguchi T, Watanabe K and Young A F 2022 *Science* **375** 774
[46] Zhang Y, Polski R, Thomson A, Lantagne-Hurtubise E, Lewandowski C, Zhou H, Watanabe K, Taniguchi T, Alicea J and Nadj-Perge S 2023 *Nature* **613** 268
[47] Tsui Y-C, He M, Hu Y, Lake E, Wang T, Watanabe K, Taniguchi T, Zaletel M P and Yazdani A 2024 *Nature* **628** 287
[48] Han T *et al* 2025 *Nature* **643** 654–61
[49] Lu Z, Han T, Yao Y, Reddy A P, Yang J, Seo J, Watanabe K, Taniguchi T, Fu L and Ju L 2024 *Nature* **626** 759
[50] Valerio Vitale A M, Atalar K and Lischner J 2022 *2D Mater.* **8** 045010
[51] Naik M H and Jain M 2018 *Phys. Rev. Lett.* **121** 266401
[52] Wu F, Lovorn T, Tutuc E, Martin I and MacDonald A H 2019 *Phys. Rev. Lett.* **122** 086402
[53] Xia Y, Han Z, Watanabe K, Taniguchi T, Shan J and Mak K F 2025 *Nature* **637** 833
[54] Guo Y *et al* 2025 *Nature* **637** 839
[55] Park H *et al* 2023 *Nature* **622** 74

[56] Goodwin Z A H and Fal'ko V 2022 *J. Phys.: Condens. Matter* **34** 494001
[57] Christopher Cheung A M, Goodwin Z A H, Han Y, Lu J, Mostofi A and Lischner J 2024 *Nano Lett.* **24** 12088–94
[58] Xian L, Kennes D M, Tancogne-Dejean N, Altarelli M and Rubio A 2019 *Nano Lett.* **19** 4934
[59] Walet N R and Guinea F 2021 *Phys. Rev. B* **103** 125427
[60] Bistritzer R and MacDonald A H 2011 *Proc. Natl Acad. Sci. USA* **108** 12233
[61] Guinea F and Walet N R 2018 *Proc. Natl Acad. Sci. USA* **115** 13174
[62] Cea T, Walet N R and Guinea F 2019 *Phys. Rev. B* **100** 205113
[63] Cea T and Guinea F 2020 *Phys. Rev. B* **102** 045107
[64] Cea T, Pantaleón P A, Walet N R and Guinea F 2022 *Nano Mater. Sci.* **4** 27
[65] Kang J and Vafek O 2018 *Phys. Rev. X* **8** 031088
[66] Koshino M, Yuan N F Q, Koretsune T, Ochi M, Kuroki K and Fu L 2018 *Phys. Rev. X* **8** 031087
[67] Goodwin Z A H, Vitale V, Corsetti F, Efetov D, Mostofi A A and Lischner J 2020 *Phys. Rev. B* **101** 165110
[68] Goodwin Z A H, Corsetti F, Mostofi A A and Lischner J 2019 *Phys. Rev. B* **100** 121106(R)
[69] Goodwin Z A H, Corsetti F, Mostofi A A and Lischner J 2019 *Phys. Rev. B* **100** 235424
[70] Gonzalez-Arraga L A, Lado J L, Guinea F and San-Jose P 2017 *Phys. Rev. Lett.* **119** 107201
[71] Lopez-Bezanilla A 2019 *Phys. Rev. Mater.* **3** 054003
[72] González J and Stauber T 2021 *Phys. Rev. B* **104** 115110
[73] Vahedi J, Peters R, Missaoui A, Honecker A and de Laissardiére G T 2021 *SciPost Phys.* **11** 083
[74] Klebl L and Honerkamp C 2019 *Phys. Rev. B* **100** 155145
[75] Klebl L, Goodwin Z A H, Mostofi A A, Kennes D M and Lischner J 2021 *Phys. Rev. B* **103** 195127
[76] Fischer A, Klebl L, Honerkamp C and Kennes D M 2021 *Phys. Rev. B* **103** L041103
[77] Jimeno-Pozo A, Goodwin Z A H, Pantaleón P A, Vitale V, Klebl L, Kennes D M, Mostofi A A, Lischner J and Guinea F 2023 *Adv. Phys. Res.* **2** 2300048
[78] Pantaleón P A, Cea T, Brown R B N R, Walet N R and Guinea F 2021 *2D Mater.* **8** 044006
[79] Wehling T O, Şaşıoğlu E, Friedrich C, Lichtenstein A I, Katsnelson M I and Blügel S 2011 *Phys. Rev. Lett.* **106** 236805
[80] Schüler M, Rösner M, Wehling T O, Lichtenstein A I and Katsnelson M I 2013 *Phys. Rev. Lett.* **111** 036601
[81] Goodwin Z A H, Vitale V, Liang X, Mostofi A A and Lischner J 2020 *Electron. Struct.* **2** 034001
[82] Cea T and Guinea F 2021 *Proc. Natl Acad. Sci. USA* **118** e2107874118
[83] Available at: https://github.com/VVitale/TBLG-U